

DNN-assisted Particle-based Bayesian Joint Synchronization and Localization

Meysam Goodarzi, Vladica Sark, Nebojsa Maletic, *Member, IEEE*, Jesús Gutiérrez, Giuseppe Caire, *Fellow, IEEE*, and Eckhard Grass

Abstract

In this work, we propose a Deep neural network-assisted Particle Filter-based (DePF) approach to address the Mobile User (MU) joint synchronization and localization (sync&loc) problem in ultra dense networks. In particular, DePF deploys an asymmetric time-stamp exchange mechanism between the MUs and the Access Points (APs), which, traditionally, provides us with information about the MUs' clock offset and skew. However, information about the distance between an AP and an MU is also intrinsic to the propagation delay experienced by exchanged time-stamps. In addition, to estimate the angle of arrival of the received synchronization packet, DePF draws on the multiple signal classification algorithm that is fed by Channel Impulse Response (CIR) experienced by the sync packets. The CIR is also leveraged on to determine the link condition, i.e. Line-of-Sight (LoS) or Non-LoS. Finally, to perform joint sync&loc, DePF capitalizes on particle Gaussian mixtures that allow for a hybrid particle-based and parametric Bayesian Recursive Filtering (BRF) fusion of the aforementioned pieces of information and thus jointly estimate the position and clock parameters of the MUs. The simulation results verifies the superiority of the proposed algorithm over the state-of-the-art schemes, especially that of Extended Kalman filter- and linearized BRF-based joint sync&loc. In particular, only drawing on the synchronization time-stamp exchange and CIRs, for 90% of the cases, the absolute position and clock offset estimation error remain below 1 meter and 2 nanoseconds, respectively.

Index Terms

5G, Joint Synchronization and Localization, Bayesian Particle Gaussian Mixture Filter, Deep Neural Network, Time-stamp exchange

M. Goodarzi, V. Sark, N. Maletic and Jesús Gutiérrez, and E.grass are with IHP – Leibniz-Institut für innovative Mikroelektronik, Frankfurt (Oder), Germany (emails: {goodarzi, sark, maletic, teran, grass}@ihp-microelectronics.com). M. Goodarzi and E. Grass are also with Humboldt University of Berlin, Germany.

G. Caire is with Technical University of Berlin (emails: caire@tu-berlin.de).

I. INTRODUCTION

The fifth generation (5G) of mobile communication networks is expected to deploy Access Points (APs) with a high spatial density to meet the increasing demand for mobile data traffic. As a result, Mobile Users (MUs) are expected to be in Line-of-Sight (LoS) of a number of APs for most of the time. Beside coping with the high demand, this also lays the ground for an accurate MU localization, which is, in particular, of crucial importance as it is the cornerstone of an enormous variety of services such as user tracking [1] and location-assisted beamforming [2]. Furthermore, such APs are likely to be equipped with antenna arrays and to support *fine time measurement* (ftm) capability introduced in several standards, e.g., IEEE 802.11 [3]. The former facilitates the Angle of Arrival (AoA) estimation while the latter allows for the AP-MU time-stamp exchange, by means of which synchronization and distance measurements are enabled. The synchronization itself also plays a decisive role when performing time-based localization. In particular, for many of the state-of-the-art MU localization techniques to function, the clock parameters of the MUs need to be known (or to be continuously tracked). Therefore, it appears that the MU's clock parameter estimation, and MU localization are closely intertwined and need to be tackled jointly.

The joint MU synchronization and localization (sync&loc) problem has been extensively addressed in the literature. The authors in [4] rely on symmetric interagent (AP-MU, inter-MU, and inter-AP) time-stamp exchange and Belief Propagation (BP) to jointly estimate MUs' location and clock offset. Furthermore, The authors of [5], [6] adopt a similar approach by means of the asymmetric time-stamp exchange mechanism proposed in [7]. While time-stamp exchange is expected to be supported in 5G networks [3], the high number of message-passings required by BP renders the approach limited in practice. Additionally, [3]–[7] provide the estimation of the sync&loc parameters at MU, whereas for the location-based services to be delivered, these parameters need to be computed on the network side. Another pitfall is the assumption they make, which is also made in [8]. That is, the network is fully cooperative, i.e., in addition to inter-AP and AP-MU communications, the MUs can also communicate to each other, what is not expected to be the case in the wireless networks. Nevertheless, the cooperation capability between the APs and the Base Stations (BSs) can be leveraged on to perform hybrid synchronization as done in [9], [10], what lays the ground for an accurate MU joint sync&loc.

Moreover, in [11], [12], the authors leverage Extended Kalman Filtering (EKF) to obtain

the estimation of clock and position parameters in ultra dense networks. In particular, they assume accurate inter-AP synchronization and perform MU joint sync&loc in the presence of uncertainty about Time of Arrival (ToA) and Angle of Arrival (AoA) parameters. The level of uncertainty is then determined based on the derived Cramer Rao Bound (CRB). Another approach called linearized BRF (L-BRF), which, similar to EKF, is based on linearizing the filter, has been employed in [13], [14], albeit the perfect inter-AP synchronization assumption is lifted. Instead, the APs and their backhauling BSs are assumed to be synchronized using cooperative hybrid synchronization introduced in [9], [10]. While EKF and L-BRF can partially mitigate the destructive impact of non-linearities in the measurements, in addition to the covariance matrix underestimation, they are likely to diverge if a reliable estimate of the initial state is not available [15]. A promising approach, on one hand, to avoid such shortcomings of EKF and, on the other hand, to boost the accuracy of position estimation, is estimating the (prediction, measurement likelihood, and posterior) distributions by means of Particle Gaussian Mixture (PGM) filters introduced in [16]. Specifically, in this approach instead of a single Gaussian function, each distribution is approximated with a sum weighted of Gaussian functions, or, alternatively, Gaussian mixtures [17]. Nevertheless, the problem that immediately arises when using PGM filters is dimensionality, rendering the approach computationally expensive for multiple variable estimations. To overcome this drawback, we resort to a hybrid parametric and particle-based approach where we capitalize on the linear relations in the measurements to reduce the dimensionality.

Even the PGM-based localization techniques can suffer from divergence under certain conditions, e.g., improper tuning of filter's hyper-parameters and faulty measurements, e.g., resulted from Non-Line-of-Sight (NLoS) links. The former must be addressed when designing the filter while the latter should be dealt with before feeding the measurements into the algorithm. In wireless networks, the most fundamental source of flawed measurements is NLoS link condition [18]. Therefore identifying the AP-MU link condition appears to be among the most vital decisions before carrying out any localization technique. To avoid such faulty measurements and the position estimation inaccuracy stemming from it, we draw on NLoS identification techniques to identify the NLoS links, drop them, and thereby boost the accuracy of the location estimation. There is a wide spectrum of NLoS identification approaches adopted in the literature, e.g. hypothesis testing as in [19], statistical approach taken in [20], and Machine Learning (ML)-based methods such as that of [21]. However, recently ML algorithms, in particular DNN-based

approaches such as AmpN introduced in [22], have drawn a huge attention for classification problems. In particular, DNNs indicate a remarkable performance due to their ability, on one hand, in implementing almost any classifier function, and, on the other hand, in extracting the task-related features from the input data [23]. The input to such networks can be the signals containing class-relevant features such as Received Signal Strength (RSS) or Channel Impulse Response (CIR). The CIR turns out to be more informative about the communication environment and link condition. Therefore, for the sake of prediction accuracy, we rely on CIRs as the input in this work.

In addition to NLoS-identification, the CIR can also be fed into one of the state-of-the-art AoA estimation algorithms to obtain the signal's direction of arrival. AoA estimation has been extensively investigated in the literature. Algorithms such as MUSIC [24], reduced-dimension MUSIC [25], and ESPRIT [26] can accurately estimate the AoA. An extensive comparison between them has been conducted in [27] and has indicated that the difference is negligible, albeit MUSIC slightly outperforms ESPRIT and, therefore, is employed for the purpose of this work.

In this paper, we propose a DNN-assisted PF-based (DePF) joint sync&loc algorithm which draws on the CIR to estimate the AoA and to determine the link condition, i.e., LoS or NLoS, thereby excluding the faulty measurements to enable a more precise parameter estimation. It then estimates the joint probability distribution of MU's clock and position parameters using the PGM filter. The dimension of the PGM filters is then reduced by revealing and exploiting the existing linearities in the measurements, thereby tackling the dimensionality problem. To the best of our knowledge, this is the first work employing PGM filter in a hybrid particle-based and parametric manner to perform joint sync&loc.

The contribution of this paper is summarized as follows:

- We present and discuss the principles of asymmetric time-stamp exchange and AoA estimation.
- We develop a DNN for NLoS identification based on AP-MU CIRs.
- We propose a DNN-assisted PF-based joint sync&loc algorithm that estimates the clock parameters and position of an MU in a hybrid parametric and particle-based manner.
- We analyze the performance of the proposed approach with the aid of detailed simulations in a challenging real-world scenario.

The rest of this paper is structured as follows: In Section II, we introduce the system model and

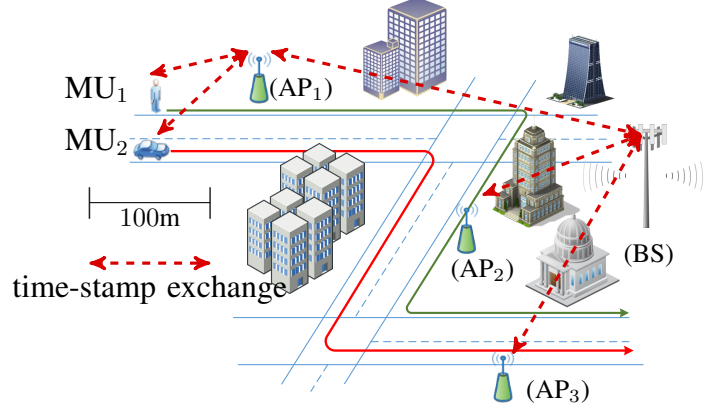


Fig. 1. An example where MU joint sync&loc can be carried out.

the preliminaries. Section III describes the details of the DePF algorithm for joint estimation of the clock and position parameters. Furthermore, simulation results are presented and discussed in Section IV. Finally, Section V concludes this work and points to future works.

Notation: The boldface capital \mathbf{A} and lower case \mathbf{a} letters denote matrices and vectors, respectively. The n -th element of vector \mathbf{a} is indicated by $\mathbf{a}[n]$. The symbol “ \bullet ” shows the inner scalar product of two (or multiple) vectors of same dimension. Moreover, \mathbf{I}_N and $\mathbf{0}_N$ represents $N \times N$ dimensional identity and all-zero matrices, respectively. $\mathbf{1}_N$ indicates an N -element all-one vector. $\mathcal{N}(\mathbf{x}|\boldsymbol{\mu}, \boldsymbol{\Sigma})$ denotes random vector \mathbf{x} distributed as Gaussian with mean vector $\boldsymbol{\mu}$ and covariance matrix $\boldsymbol{\Sigma}$. A diagonal matrix with the diagonal elements (x_1, \dots, x_K) is denoted by $\text{diag}(x_1, \dots, x_K)$. Symbol \sim stands for “is distributed as” and the symbol \propto represents the linear scalar relationship between two real-valued functions.

II. SYSTEM MODEL AND PRELIMINARIES

We consider a network of multiple APs with known locations, all backhauled by BSs. The APs are assumed to feature Uniform Planar Arrays (UPAs), which allow for accurate azimuth and elevation AoA estimations, and to be able to continuously synchronize themselves with the backhauling BSs using the hybrid synchronization algorithm described in [9], [14]. This, in particular, guarantees a low time error among the neighboring APs, enabling a more precise cooperative localization. A further assumption is that, at each sync&loc period T , a set of APs denoted by \mathcal{I}_i , are able to periodically exchange time-stamps with the i -th MU using the ftm feature embedded in the communication devices and implemented by an existing protocol, e.g.,

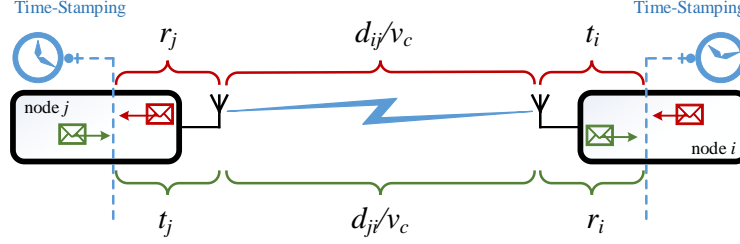


Fig. 2. Decomposition of the clock offset into its constituent components.

PTP [28]. From the packet containing these time-stamps, the APs can also estimate the CIRs and AoA. The AP-MU link condition is considered to be both LoS and NLoS for the sake of thoroughness. Nevertheless, it is known from [29], that for such a scenario the LoS probability is around 0.8, even growing to 0.95 when the AP density is 40 meters. A DNN trained by means of CIRs is employed to distinguish the LoS condition from NLoS, permitting the localization unit to neglect the measurements conducted under NLoS condition, thereby augmenting the accuracy of synchronization and localization. In what follows, we firstly present the clock model for the APs and the MUs. Then, we explain the time-stamp exchange mechanism in detail. Subsequently, we discuss the DNN that allows for a reliable NLoS/LoS identification. Lastly, the principles of MUSIC algorithm are briefly described.

A. Clock Model

We consider the following clock model for each node i .

$$c_i(t) = \gamma_i t + \theta_i, \quad (1)$$

where t represents the global reference time. Furthermore, γ_i and θ_i denote the clock skew and offset, respectively. Although, the parameter γ_i is generally random and time-varying, it is common to assume that it remains constant in the course of one synchronization period T [30]–[32]. Given that, the first goal of the joint sync&loc algorithm is to estimate and track the clock parameters γ_i and θ_i (or transformations thereof) for each MU.

B. Offset Decomposition and Time-stamp Exchange

1) *Offset decomposition:* To elaborate on the constituents of the offset θ_i , we break it down as shown in Figure 2. The parameter t_j/t_i is the time taken for a packet to leave the transmitter

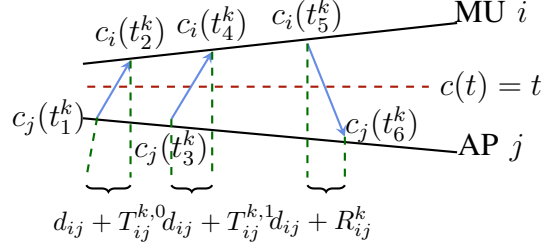


Fig. 3. Time-stamp exchange between MU i and AP j . Blue/red solid/dashed lines indicate the active/passive listening of AP j .

after being time-stamped, d_{ji}/d_{ij} represents the distance between the nodes j/i and i/j , v_c is the speed of light, and r_i/r_j represents the time that a packet needs to reach the time-stamping point upon arrival at the receiver. Generally, the packets sent from node j to node i do not necessarily experience the same delay as those sent from node i to node j . In other words,

$$t_j + \frac{d_{ji}}{v_c} + r_i \neq t_i + \frac{d_{ij}}{v_c} + r_j.$$

The variables $T_{ij} = t_j + r_i$, and $R_{ij} = t_i + r_j$ (and correspondingly t_j , t_i , r_j , and r_i), are random variables due to multiple hardware-related random independent processes and can, therefore, be assumed i.i.d. Gaussian random variables, whereas d_{ji} and d_{ij} are usually assumed to be deterministic and symmetric ($d_{ji} = d_{ij}$) [1], [31]. The random variables T_{ij} and R_{ij} are assumed to be distributed as $\mathcal{N}(\mu_T, \sigma_T^2)$ and $\mathcal{N}(\mu_R, \sigma_R^2)$, respectively. As mentioned in [30], [31], [33], while it is typical to assume that $\mu_T = \mu_R$, and parameters σ_T and σ_R are known, having any information about the value of μ_T and μ_R is highly unlikely. Therefore, we construct the joint sync&loc algorithm assuming no knowledge on μ_T and μ_R except for $\mu_T = \mu_R$.

2) *Time-stamp exchange mechanism:* We draw on the asymmetric time-stamp exchange mechanism shown in Figure 3, proposed in [7], and employed in [5], [30]. Node j transmits a *sync* message wherein the local time $c_j(t_1^k)$ is incorporated. Node i receives the packet and records the local reception time $c_i(t_2^k)$. After a certain time, the process repeats again with $c_j(t_3^k)$ and $c_i(t_4^k)$. Subsequently, at local time $c_i(t_5^k)$, node i sends back a *sync* message to node j with $c_i(t_2^k)$, $c_i(t_4^k)$ and $c_i(t_5^k)$ incorporated. Upon reception, node j records the local time $c_j(t_6^k)$. Finally, at the k -th round of time-stamp exchange (and correspondingly k -th round of joint sync&loc), the localization unit is expected to have collected the time-stamps

$$\mathbf{c}_{ij}^k = [c_j(t_1^k), c_i(t_2^k), c_j(t_3^k), c_i(t_4^k), c_i(t_5^k), c_j(t_6^k)].$$

The collected time-stamps will be exploited in Section III to design a joint sync&loc algorithm.

C. NLoS Identification and Channel Impulse Response

The capability to estimate CIR is highly ubiquitous among the APs. Given that, relying on the CIR to develop localization algorithms appears to be a realistic approach. In fact, the AP-MU CIR is a rich source of information about the condition of the communication link, e.g., LoS or NLoS, and the location of the MU. More precisely, the former is crucial to know when estimating the latter as the reliability of the distance, or alternatively time, and AoA measurements significantly sinks if conducted under NLoS condition.

Furthermore, DNN units are also expected to be a part of communication devices as they are the cornerstone of many solutions for different communication problems such as slice management and anomaly detection [34]. Apart from that, in the applications of this type, i.e., classification problems, DNN is proven to have a superb performance due its remarkable ability to extract the class-relevant features which eventually paves the way towards an accurate prediction [35]. On the contrary, other approaches such as Support Vector Machine (SVM), or Bayesian sequential test requires human intervention that may be, given the limited intuition, flawed and erroneous.

Figure 4 shows the general architecture of the DNN deployed for the purpose of NLoS-identification. It consists of an input layer with one channel receiving N samples, i.e. the magnitude of the CIR. The number of hidden layers and neurons in each hidden layer are set to l_H and n_H , respectively. The rationale to rely on when selecting these numbers is that, according to [23], any classifier function can be realized by two hidden layers, i.e. currently there is no theoretical reason to use more than two. However, the lack of evidence does not imply that the DNNs with more hidden layers do not improve the accuracy of classification, it rather suggests that the number of required hidden layers does not follow a well-established logic and it is mostly determined by a trial-and-error process. Therefore, for the algorithm proposed in this work, we empirically determine the l_H that delivers the best performance. Furthermore, as a rule of thumb, the number of neurons is suggested be between the number of the inputs and that of the outputs to prevent under/overfitting.

Let $\zeta^i \triangleq [\hat{p}_{\text{los}}, \hat{p}_{\text{nlos}}]$ be the DNN's output probability vector, where \hat{p}_{los} and \hat{p}_{nlos} denote the probability of the i -th CIR being corresponded to a LoS link and an NLoS link, respectively. It is straightforward to see that $\hat{p}_{\text{los}} = 1 - \hat{p}_{\text{nlos}}$. For the NLoS-identifier, we seek to train the DNN such that the output value of vector ζ is as close as possible to the $[1, 0]/[0, 1]$ for the LoS/NLoS

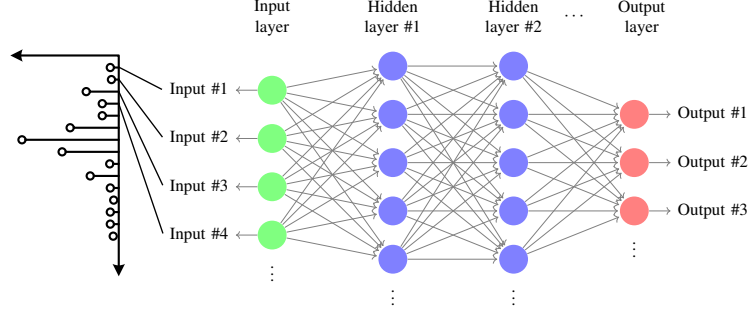


Fig. 4. DNN architecture employed to perform NLoS-identification.

CIRs. In other words, from the optimization point of view, we aim to design a loss function whose output is small when the DNN returns the ζ correctly, and is large otherwise. It turns out that the function that possesses the above-mentioned property is the logarithmic function [36]. Mathematically, the loss function is given by [35]

$$L_c = -\frac{1}{M_c} \sum_{i=1}^{M_c} p_{\text{los}}^i \log(\hat{p}_{\text{los}}^i) + p_{\text{nlos}}^i \log(\hat{p}_{\text{nlos}}^i) = -\frac{1}{M_c} \sum_{i=1}^{M_c} p_{\text{los}}^i \log(\hat{p}_{\text{los}}^i) + (1 - p_{\text{los}}^i) \log(1 - \hat{p}_{\text{los}}^i), \quad (2)$$

where p_{los}^i and p_{nlos}^i denote the label corresponding to the i -th CIR sample in the data set. The formulation in (2) is also known in the literature as binary cross-entropy loss function. The goal of training is then to adjust the weights of the neurons such that (2) is minimized.

D. Angle of Arrival

The CIR fed into the DNN to identify the link condition can be treated as an input signal to the MUSIC algorithm to obtain the AoA. In the sequel, we present the principles of AoA estimation for UPAs based on [37]–[39]. The estimated AoA is given by

$$(\varphi_{ij}, \alpha_{ij}) = \arg \max_{\varphi, \alpha} \frac{1}{\mathbf{a}_n(\varphi, \alpha)^H \mathbf{N} \mathbf{N}^H \mathbf{a}_n(\varphi, \alpha)}, \quad (3)$$

where φ_{ij} and α_{ij} are the azimuth and elevation AoA of the signal received from the MU i at AP j , respectively. Parameter $\mathbf{a}_n(\varphi, \alpha)$ is the signal vector rotation on the n -th subcarrier and is

given by

$$\mathbf{a}_n(\varphi, \alpha) = \begin{bmatrix} 1 \\ e^{i\frac{2\pi d}{\lambda} \sin(\alpha)(\sin(\varphi)+\cos(\varphi))} \\ e^{i\frac{2\pi d}{\lambda} \sin(\alpha)(\sin(\varphi)+2\cos(\varphi))} \\ \vdots \\ e^{i\frac{2\pi d}{\lambda} \sin(\alpha)((N_{\text{ant}}-1)\sin(\varphi)+(N_{\text{ant}}-2)\cos(\varphi))} \\ e^{i\frac{2\pi d}{\lambda} (N_{\text{ant}}-1) \sin(\alpha)(\sin(\varphi)+\cos(\varphi))} \end{bmatrix}_{N_{\text{ant}}^2 \times 1}, \quad (4)$$

where N_{ant} denotes the number of AP antennas in one row (or column). Matrix \mathbf{N} is constructed by $N_{\text{ant}}^2 - 1$ most right columns of the eigenvectors obtained when performing eigen decomposition of the covariance matrix of the received signal. That is

$$\mathbf{R} = \mathbf{V}\mathbf{A}\mathbf{V}^H, \quad (5)$$

where matrices \mathbf{A} and \mathbf{V} contain the eigenvalues and eigenvectors, respectively. Furthermore,

$$\mathbf{R} = \frac{1}{N_s} \sum_{n=1}^{N_s} \mathbf{x}_n \mathbf{x}_n^H, \quad (6)$$

where the vector \mathbf{x}_n is of dimension $N_{\text{ant}}^2 \times 1$ and represents the n -th elements of FFT of the CIRs. It is worth mentioning that, when constructing \mathbf{N} , the eigen decomposition in (5) is assumed to sort the eigenvalues in a decreasing order. Furthermore, we note that, each AP is assumed to have N_{ant}^2 CIRs at its disposal.

III. CLOCK PARAMETERS AND POSITION ESTIMATION

In this section, we discuss the clock and position estimation method. It relies primarily on the AoA estimation, NLoS identification, time-stamp collected in the previous section. In particular, given Section II-B2, and considering AP j as master node, we can write

$$\frac{1}{\tilde{\gamma}_i} (c_i(t_2^k) - \tilde{\theta}_i) = c_j(t_1^k) + \frac{d_{ij}}{v_c} + T_{ij}^{k,0}, \quad (7)$$

$$\frac{1}{\tilde{\gamma}_i} (c_i(t_4^k) - \tilde{\theta}_i) = c_j(t_3^k) + \frac{d_{ij}}{v_c} + T_{ij}^{k,1}, \quad (8)$$

$$\frac{1}{\tilde{\gamma}_i} (c_i(t_5^k) - \tilde{\theta}_i) = c_j(t_6^k) - \frac{d_{ij}}{v_c} - R_{ij}^k, \quad (9)$$

where t_1^k/t_2^k , t_3^k/t_4^k , and t_5^k/t_6^k are the time points where MU i and AP j send/receive the sync messages, respectively. Parameter $d_{ij} = \sqrt{(x_i - x_j)^2 + (y_i - y_j)^2}$ denotes the Euclidean distance between nodes i and j . We note that, In Figure 3, instead of a global time reference $c(t) = t$,

we take node j as master node. It is straightforward to see that $\frac{1}{\tilde{\gamma}_i} = \frac{\gamma_j}{\gamma_i}$, $\tilde{\theta}_i = \theta_i - \tilde{\gamma}_i \theta_j$, $\tilde{d}_{ij} + \tilde{T}_{ij}^k = \gamma_j(d_{ij} + T_{ij}^k)$, and $\tilde{d}_{ij} - \tilde{R}_{ij}^k = \gamma_j(d_{ij} - R_{ij}^k)$. For the sake of simplicity, as done in [1], we assume $\tilde{d}_{ij} = d_{ij}$, $\tilde{R}_{ij}^k = R_{ij}^k$, and $\tilde{T}_{ij}^k = T_{ij}^k$. This is valid because $\gamma_j \approx 1$ and the values of $d_{ij} + T_{ij}^k$ and $d_{ij} - R_{ij}^k$ are low. In what follows, we firstly give the probabilistic representation of the problem. Subsequently, the principles of the estimation method are presented.

A. Probabilistic Formulation of the Problem

Let ξ_i^k be the state of the vector variable $\xi_i \triangleq [\tilde{\boldsymbol{\theta}}_i \quad \mathbf{p}_i]^T$ after the k -th round of time-stamp exchange, where $\tilde{\boldsymbol{\theta}}_i = [\frac{1}{\tilde{\gamma}_i} \quad \frac{\tilde{\theta}_i}{\tilde{\gamma}_i}]$ and $\mathbf{p}_i = [x_i \quad y_i]$. Parameters x_i and y_i denote the position of node i on the x and y axis, respectively. The aim is then to infer the *probability distribution function* (pdf) corresponding to the k -th state, which can be written as

$$p(\xi_i^k | \{\mathbf{c}_{ij}^{1:k}, \varphi_{ij}^{1:k}, \zeta_{ij}^{1:k}\}_{\forall j \in \mathcal{I}_i}) = \int p(\xi_i^0, \dots, \xi_i^k | \{\mathbf{c}_{ij}^{1:k}, \varphi_{ij}^{1:k}, \zeta_{ij}^{1:k}\}_{\forall j \in \mathcal{I}_i}) d\xi_i^0 \dots d\xi_i^{k-1}, \quad (10)$$

where the superscript $1:k$ indicates the collection of measurements from the first round until the k -th. Applying Bayesian rule, we can rewrite (10) as

$$p(\xi_i^k | \{\mathbf{c}_{ij}^{1:k}, \varphi_{ij}^{1:k}, \zeta_{ij}^{1:k}\}_{\forall j \in \mathcal{I}_i}) \propto \int p(\{\mathbf{c}_{ij}^{1:k}, \varphi_{ij}^{1:k}, \zeta_{ij}^{1:k}\}_{\forall j \in \mathcal{I}_i} | \xi_i^0, \dots, \xi_i^k) p(\xi_i^0, \dots, \xi_i^k) d\xi_i^0 \dots d\xi_i^{k-1}. \quad (11)$$

Figure 5 depicts the temporal evolution of ξ_i^k as well as its relation with the measurements at each time step. Such a structure is referred to as Dynamic Bayesian Network (DBN), in which a basic Bayesian Network (BN) repeats itself in each time step [40]. The states of a DBN, i.e., all the variables with the same time index, satisfy the Markov property¹ [41], enabling us to carry out the mathematical simplification as in the Appendix A, which leads to

$$p(\xi_i^k | \{\mathbf{c}_{ij}^{1:k}, \varphi_{ij}^{1:k}, \zeta_{ij}^{1:k}\}_{\forall j \in \mathcal{I}_i}) \propto p(\xi_i^k | \{\mathbf{c}_{ij}^{1:k-1}, \varphi_{ij}^{1:k-1}, \zeta_{ij}^{1:k-1}\}_{\forall j \in \mathcal{I}_i}) p(\mathbf{c}_{ij}^k, \varphi_{ij}^k, \zeta_{ij}^k | \xi_i^k). \quad (12)$$

The term $p(\xi_i^k | \{\mathbf{c}_{ij}^{1:k-1}, \varphi_{ij}^{1:k-1}, \zeta_{ij}^{1:k-1}\}_{\forall j \in \mathcal{I}_i})$ is referred to as *prediction* step while the term $p(\mathbf{c}_{ij}^k, \varphi_{ij}^k, \zeta_{ij}^k | \xi_i^k)$ is considered as *correction* step [41]. If the Gaussian assumption about ξ_i^0 held and the relation between all the states in Figure 5 were linear, we could conclude that the marginal in (12) would also be Gaussian distributed. Unfortunately, that is not the case in the joint sync&loc problem as the measurement equations (and consequently the correction steps) are partially non-linear. In concrete terms, the aforementioned problem stems from the non-linear

¹It postulates that, the state of the system at time t depends only on its immediate past, i.e. its state at time $t - 1$.

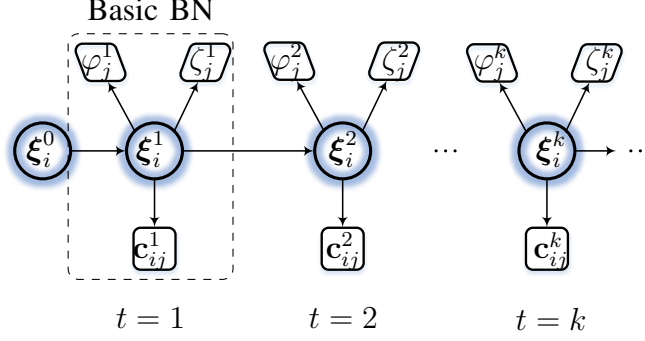


Fig. 5. Dynamic Bayesian network representing the temporal evolution of the vector variable ξ_i and its relation with the measurements.

relation between the location parameters (x_i, y_i) and the time-stamps in (7), (8), (9) on one hand, and the measured AoA in (3) on the other hand.

There are several approaches to tackle the non-linearity problem and, consequently, to estimate the non-Gaussian posterior distribution. In [13], it is proposed to undertake the Taylor expansion of the non-linear terms around the prediction point, while [11], [12], [42] have employed EKF to address the non-linearity. In addition to being prone to divergence, which is hard to mitigate analytically, all of these methods require initialization and even then are only able to deliver medium accuracy. In what follows, we discuss the details of a novel joint sync&loc approach based on PGM filters.

B. Particle Gaussian Mixure Filter

The idea underpinning PGM filters is to approximate a posterior pdf by the sum of weighted *Gaussian density functions* (gdfs) [16]. Leveraging on this idea, we can write the posterior in (12) as

$$p(\xi_i^k | \{c_{ij}^{1:k}, \varphi_{ij}^{1:k}, \zeta_{ij}^{1:k}\}_{\forall j \in \mathcal{I}_i}) = \sum_{f=1}^F w_f^k \mathcal{N}(\xi_i^k | \mu_f^k, \Sigma_f^k), \quad \text{with} \quad \sum_{f=1}^F w_f^k = 1, \quad w_f^k \geq 0 \quad \forall f, \quad (13)$$

where $\mu_f^k = [\mu(\tilde{\mathbf{v}}_i)_f^k \quad \mu(\mathbf{p}_i)_f^k]$ and $\Sigma_f^k = \begin{bmatrix} \Sigma(\tilde{\mathbf{v}}_i)_f^k & \mathbf{0}_2 \\ \mathbf{0}_2 & \Sigma(\mathbf{p}_i)_f^k \end{bmatrix}$ denote the mean vector and covariance matrix of the f -th gdf in the k -th round of estimation, respectively. Parameter F represents the total number of gdfs. Furthermore, $\mu(\tilde{\mathbf{v}}_i)_f^k / \mu(\mathbf{p}_i)_f^k$ and $\Sigma(\tilde{\mathbf{v}}_i)_f^k / \Sigma(\mathbf{p}_i)_f^k$ represent the mean vector and covariance matrix corresponding to the vector variable $\tilde{\mathbf{v}}_i / \mathbf{p}_i$, respectively.

Seeking to further simplify (13), we reformulate (7), (8), and (9) as follows. Subtracting (7) from (8) leads to

$$\frac{1}{\tilde{\gamma}_i}(c_i(t_4^k) - c_i(t_2^k)) = c_j(t_3^k) - c_j(t_1^k) + T_{ij}^{k,1} - T_{ij}^{k,0}, \quad (14)$$

while summing up (8) and (9)

$$\frac{1}{\tilde{\gamma}_i}(c_i(t_4^k) + c_i(t_5^k) - 2\tilde{\theta}_i) = c_j(t_3^k) + c_j(t_6^k) + T_{ij}^{k,1} - R_{ij}^k. \quad (15)$$

It is straightforward to observe that $\tilde{\boldsymbol{\theta}}_i^k$, on one hand, is linearly dependent on the time-stamps, and, on the other hand, does not depend on \mathbf{p}_i . This suggests that, although the $p(\mathbf{c}_{ij}^k, \varphi_{ij}^k, \zeta_{ij}^k | \boldsymbol{\xi}_i^k)$ is not Gaussian distributed in general, it is indeed Gaussian across the $\tilde{\boldsymbol{\theta}}_i$ axis as both T_{ij} and R_{ij} are Gaussian distributed. In fact, we capitalize on the linear Gaussian substructures in the model to keep the state dimensions low. Consequently, the gdfs can be employed only across the \mathbf{p}_i axis transforming the structure of (13) into multiplication of a single gdf across $\tilde{\boldsymbol{\theta}}_i$ and sum weighted of multiple gdfs across \mathbf{p}_i (visualized in Figure 6). Such a structure not only lays the ground for the hybrid parametric and particle-based implementation of BRF-based joint sync&loc estimation, but also dramatically reduces the computational burden. Given above, (13) can be simplified as

$$p(\{\mathbf{c}_{ij}^{1:k}, \varphi_{ij}^{1:k}, \zeta_{ij}^{1:k}\}_{\forall j \in \mathcal{I}_i} | \boldsymbol{\xi}_i^k) = \mathcal{N}(\tilde{\boldsymbol{\theta}}_i^k | \boldsymbol{\mu}(\tilde{\boldsymbol{\theta}}_i)^k, \boldsymbol{\Sigma}(\tilde{\boldsymbol{\theta}}_i)^k) \sum_{f=1}^F w_f^k \mathcal{N}(\mathbf{p}_i^k | \boldsymbol{\mu}(\mathbf{p}_i)_f^k, \boldsymbol{\Sigma}(\mathbf{p}_i)_f^k). \quad (16)$$

We note that when $\boldsymbol{\Sigma}(\mathbf{p}_i)_f^k$ approaches 0, the term $\mathcal{N}(\mathbf{p}_i^k | \boldsymbol{\mu}(\mathbf{p}_i)_f^k, \boldsymbol{\Sigma}(\mathbf{p}_i)_f^k)$ tends towards $\delta(\mathbf{p}_i^k - \boldsymbol{\mu}(\mathbf{p}_i)_f^k)$, where $\delta(\cdot)$ denote the Dirac impulse function. Such a function forms the basis of the classical particle filter. In what follows, we further delve into the steps of parameter estimation of the above-mentioned distribution. Firstly, the details of *prediction* step are described, where all the parameters are denoted by $(\cdot)_-$. Next, we obtain the likelihood of the measurements whose parameters are represented by $(\cdot)_+$. Lastly, we compute the parameters of the posterior distribution in (16) and perform the resampling.

1) *Prediction*: Given the linear dynamics of MUs' clocks and movements, a reasonable prediction for $\boldsymbol{\xi}_i^k$ is given by

$$p(\boldsymbol{\xi}_i^k | \{\mathbf{c}_{ij}^{1:k-1}, \varphi_{ij}^{1:k-1}, \zeta_{ij}^{1:k-1}\}_{\forall j \in \mathcal{I}_i}) = \mathcal{N}(\tilde{\boldsymbol{\theta}}_i^k | \boldsymbol{\mu}(\tilde{\boldsymbol{\theta}}_i)_-, \boldsymbol{\Sigma}(\tilde{\boldsymbol{\theta}}_i)_-) \sum_{f=1}^F w_{f-}^k \mathcal{N}(\mathbf{p}_i^k | \boldsymbol{\mu}(\mathbf{p}_i)_{f-}^k, \boldsymbol{\Sigma}(\mathbf{p}_i)_{f-}^k) \quad (17)$$

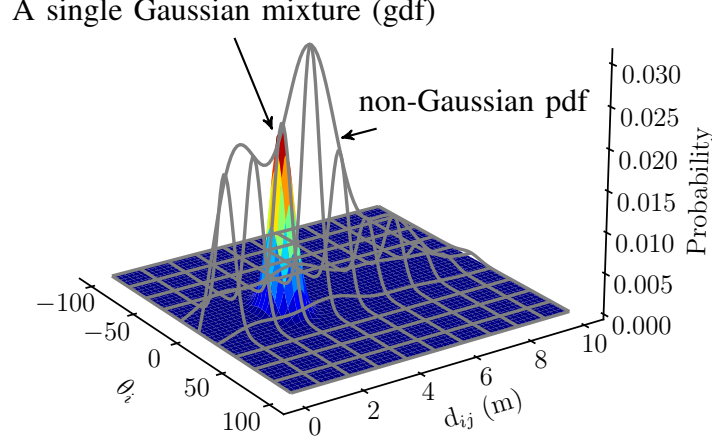


Fig. 6. An example distribution of the ξ_i for a given time-stamp measurement.

where

$$w_{f-}^k = \frac{1}{F} \mathbf{1}_F, \quad \boldsymbol{\mu}(\mathbf{p}_i)_{f-}^k = \boldsymbol{\mu}(\mathbf{p}_i)_f^{k-1} + \mathbf{n}_f,$$

with \mathbf{n}_f being the noise vector derived from the distribution $\mathcal{N}(\mathbf{n}|0, \mathbf{Q}_n(\mathbf{p}_i))$, for $\mathbf{Q}_n(\mathbf{p}_i) = \text{diag}(\sigma_x^2, \sigma_y^2)$. In practice, we initialize $\boldsymbol{\Sigma}(\mathbf{p}_i)_{f-}^k \propto \text{diag}(F^{-0.4}, F^{-0.4})$, which is proved in [15] to be the optimal choice. Furthermore, according to [9],

$$\boldsymbol{\mu}(\tilde{\boldsymbol{\vartheta}}_i)_-^k = \mathbf{F} \boldsymbol{\mu}(\tilde{\boldsymbol{\vartheta}}_i)^{k-1} + \mathbf{u}, \quad \boldsymbol{\Sigma}(\tilde{\boldsymbol{\vartheta}}_i)_-^k = \mathbf{F} \boldsymbol{\Sigma}(\tilde{\boldsymbol{\vartheta}}_i)^{k-1} \mathbf{F}^T + \mathbf{Q}_n(\tilde{\boldsymbol{\vartheta}}_i) \quad (18)$$

with

$$\mathbf{F} = \begin{bmatrix} 1 & 0 \\ T & 1 \end{bmatrix}, \quad \mathbf{u} = \begin{bmatrix} 0 & T \end{bmatrix}^T, \quad \mathbf{Q}_n(\tilde{\boldsymbol{\vartheta}}_i) = \text{diag}(\sigma_\gamma^2, \sigma_\theta^2).$$

The matrices $\mathbf{Q}_n(\tilde{\boldsymbol{\vartheta}}_i)$ and $\mathbf{Q}_n(\mathbf{p}_i)$ denote the covariance of the zero-mean Gaussian noises on each gdf across the $\tilde{\boldsymbol{\vartheta}}_i$ and \mathbf{p}_i axes, respectively. In general, the design of $\mathbf{Q}_n(\cdot)$ is a difficult task. In particular, if it is too small, the filter will be overconfident in its prediction model and will diverge from the actual solution. In contrast, if it is too large, it will be unduly dominated by the noise in the measurements and perform sub-optimally [43]. Similar to [1], [30], [32], we set σ_γ^2 and σ_θ^2 , such that the external noises as well as the residues from the previous iteration are accounted for. Furthermore, to determine the value of σ_x^2 and σ_y^2 , the design model discussed in [42], [43] is followed. That is, opting for a noise variance that is large enough to allow the gdfs to assign a reasonable probability to the locations where the MU might be. In the urban scenario for example, the maximum permitted speed is 50 km/h (≈ 14 m/s), resulting in $\sigma_x = \sigma_y = 14 \times T$.

2) *Measurement Likelihood and Weight Update:* The same structure as (16) is imposed on the likelihood of the measurements. That is,

$$p(\mathbf{c}_{ij}^k, \varphi_{ij}^k, \zeta_{ij}^k | \boldsymbol{\xi}_i^k) = \mathcal{N}(\tilde{\boldsymbol{\vartheta}}_i^k | \boldsymbol{\mu}(\tilde{\boldsymbol{\vartheta}}_i^k)_+, \boldsymbol{\Sigma}(\tilde{\boldsymbol{\vartheta}}_i^k)_+) \sum_{f=1}^F w_{f+}^k \mathcal{N}(\mathbf{p}_i^k | \boldsymbol{\mu}(\mathbf{p}_i^k)_{f+}^k, \boldsymbol{\Sigma}(\mathbf{p}_i^k)_{f+}^k) \quad (19)$$

To obtain the parameters of the above likelihood, we firstly transform (14) and (15) into the matrix form. That is,

$$\mathbf{B}_{ij}^k \tilde{\boldsymbol{\vartheta}}_i^k = \mathbf{r}_{ij}^k + \mathbf{z}_{ij}, \quad (20)$$

where $\mathbf{z}_{ij} \sim \mathcal{N}(\mathbf{z} | \mathbf{0}, \mathbf{R}_{ij}^k)$ with $\mathbf{R}_{ij}^k = \text{diag}(2\sigma_{T_{ij}}^2, \sigma_{T_{ij}}^2 + \sigma_{R_{ij}}^2)$, and

$$\mathbf{B}_{ij}^k = \begin{bmatrix} c_i(t_4^k) - c_i(t_2^k) & 0 \\ c_i(t_4^k) + c_i(t_5^k) & -2 \end{bmatrix}, \mathbf{r}_{ij}^k = \begin{bmatrix} c_j(t_3^k) - c_j(t_1^k) \\ c_j(t_3^k) + c_j(t_6^k) \end{bmatrix}.$$

The mean and covariance matrix of the gdfs across the $\tilde{\boldsymbol{\vartheta}}_i$ axis can be written as

$$\boldsymbol{\mu}(\tilde{\boldsymbol{\vartheta}}_i)_+^k = \mathbf{A}_{ij}^k \mathbf{r}_{ij}^k, \quad \boldsymbol{\Sigma}(\tilde{\boldsymbol{\vartheta}}_i)_+^k = \mathbf{A}_{ij}^k \mathbf{R}_{ij}^k (\mathbf{A}_{ij}^k)^T, \quad (21)$$

where $\mathbf{A}_{ij}^k = ((\mathbf{B}_{ij}^k)^T \mathbf{B}_{ij}^k)^{-1} (\mathbf{B}_{ij}^k)^T$.

To obtain the location parameters corresponding to each gdf, we can assume that measurement equations are linear in the vicinity of the point predicted by the prediction step. That is, to approximate them with their first-order Taylor expansion, the details of which are thoroughly explained in [13], [14]². The measurement equations we rely on to estimate the parameters of the likelihoods are (9) and

$$\arctan\left(\frac{y_i - y_j}{x_i - x_j}\right) = \varphi_{ij}^k, \quad (22)$$

where φ_{ij}^k is calculated as explained in Section II-D. Carrying out the necessary mathematical manipulation, we can write the same relation as (20) for each gdf. That is,

$$\mathbf{B}_{ij,f}^k \mathbf{p}_i^k = \mathbf{r}_{ij,f}^k + \mathbf{z}_{ij,f}, \quad (23)$$

where $\mathbf{z}_{ij,f} \sim \mathcal{N}(\mathbf{z} | \mathbf{0}, \mathbf{R}_{ij,f})$ with $\mathbf{R}_{ij,f} = \text{diag}(\sigma_{R_{ij}}^2, \sigma_{\varphi}^2)$. Furthermore,

$$\mathbf{B}_{ij,f} = \begin{bmatrix} \mathbf{a}_j^k \\ \mathbf{b}_j^k \end{bmatrix}$$

with the vectors \mathbf{a}_j^k and \mathbf{b}_j^k calculated by means of (24) and (25), respectively. Finally, $\mathbf{r}_{ij,f}$ is constructed as in (26). We note that (24) and (25) are computed by means of the Taylor

²Note that this is equivalent to EKF, e.g. that of [42]. Nevertheless, to keep the consistency with the approach taken in this work, i.e. Bayesian representation of the filtering process, we avoid using EKF representation.

$$a_{j,f}^k = \frac{1}{v_c} \left| \boldsymbol{\mu}(\mathbf{p}_i)_{f-}^k - \mathbf{p}_j \right|, \quad \mathbf{a}_{j,f}^k = \frac{1}{v_c^2 a_{j,f}^k} \left(\boldsymbol{\mu}(\mathbf{p}_i)_{f-}^k - \mathbf{p}_j \right), \quad (24)$$

$$b_{j,f}^k = \arctan\left(\frac{\mathbf{a}_{j,f}^k[2]}{\mathbf{a}_{j,f}^k[1]}\right), \quad \mathbf{b}_{j,f}^k = \frac{1}{a_{j,f}^k} \begin{bmatrix} -\mathbf{a}_{j,f}^k[2], & \mathbf{a}_{j,f}^k[1] \end{bmatrix}. \quad (25)$$

$$\mathbf{r}_{ij,f} = \left[c_j(t_6^k) - a_{j,f}^k + \boldsymbol{\mu}(\mathbf{p}_i)_{f-}^k \bullet \mathbf{a}_{j,f}^k - \begin{bmatrix} c_i(t_5^k) & -1 \end{bmatrix} \bullet \boldsymbol{\mu}(\tilde{\boldsymbol{\vartheta}}_i)_+^k, \quad \varphi_{ij}^k - b_{j,f}^k + \boldsymbol{\mu}(\mathbf{p}_i)_{f-}^k \bullet \mathbf{b}_{j,f}^k \right]^T. \quad (26)$$

expansion of (9) and (22) around the predicted point $\boldsymbol{\mu}(\mathbf{p}_i)_{f-}^k$ with the known $\boldsymbol{\mu}(\tilde{\boldsymbol{\vartheta}}_i)_+^k$ obtained by (21). Given (23) (and similar to (21)) we can write

$$\boldsymbol{\mu}(\mathbf{p}_i)_{f+}^k = \mathbf{A}_{ij,f}^k \mathbf{r}_{ij,f}^k, \quad \boldsymbol{\Sigma}(\mathbf{p}_i)_{f+}^k = \mathbf{A}_{ij,f}^k \mathbf{R}_{ij,f}^k (\mathbf{A}_{ij,f}^k)^T, \quad (27)$$

where $\mathbf{A}_{ij,f}^k = ((\mathbf{B}_{ij,f}^k)^T \mathbf{B}_{ij,f}^k)^{-1} (\mathbf{B}_{ij,f}^k)^T$. Furthermore, it is straightforward to see that

$$w_{f+}^k = \mathcal{N}(\mathbf{p}_i = \boldsymbol{\mu}(\mathbf{p}_i)_{f+}^k | \boldsymbol{\mu}(\mathbf{p}_i)_{f+}^k, \boldsymbol{\Sigma}(\mathbf{p}_i)_{f+}^k). \quad (28)$$

In other words, the weights are equal to the likelihood of the mean of each gdf.

3) *Posterior Estimation:* Having taken the necessary steps, we can now compute (16) as an approximation for the posterior distribution in (12). Multiplying (17) and (19), the parameters of (16) can be given by

$$\boldsymbol{\mu}(\tilde{\boldsymbol{\vartheta}}_i)^k = \left[\boldsymbol{\Sigma}(\tilde{\boldsymbol{\vartheta}}_i)_-^k + \boldsymbol{\Sigma}(\tilde{\boldsymbol{\vartheta}}_i)_+^k \right]^{-1} \left(\boldsymbol{\Sigma}(\tilde{\boldsymbol{\vartheta}}_i)_+^k \boldsymbol{\mu}(\tilde{\boldsymbol{\vartheta}}_i)_-^k + \boldsymbol{\Sigma}(\tilde{\boldsymbol{\vartheta}}_i)_-^k \boldsymbol{\mu}(\tilde{\boldsymbol{\vartheta}}_i)_+^k \right), \quad (29)$$

$$\boldsymbol{\Sigma}(\tilde{\boldsymbol{\vartheta}}_i)^k = \left[\left(\boldsymbol{\Sigma}(\tilde{\boldsymbol{\vartheta}}_i)_-^k \right)^{-1} + \left(\boldsymbol{\Sigma}(\tilde{\boldsymbol{\vartheta}}_i)_+^k \right)^{-1} \right]^{-1}. \quad (30)$$

The final estimation of the clock skew and offset can then be given by

$$\tilde{\gamma}_i^k = \frac{1}{\boldsymbol{\mu}(\tilde{\boldsymbol{\vartheta}}_i)^k[1]}, \quad \tilde{\theta}_i^k = \frac{\boldsymbol{\mu}(\tilde{\boldsymbol{\vartheta}}_i)^k[2]}{\boldsymbol{\mu}(\tilde{\boldsymbol{\vartheta}}_i)^k[1]}. \quad (31)$$

Furthermore, each gdf can be updated across \mathbf{p}_i axis by

$$\boldsymbol{\mu}(\mathbf{p}_i)_f^k = \left[\boldsymbol{\Sigma}(\mathbf{p}_i)_{f-}^k + \boldsymbol{\Sigma}(\mathbf{p}_i)_{f+}^k \right]^{-1} \times \left(\boldsymbol{\Sigma}(\mathbf{p}_i)_{f+}^k \boldsymbol{\mu}(\mathbf{p}_i)_{f-}^k + \boldsymbol{\Sigma}(\mathbf{p}_i)_{f-}^k \boldsymbol{\mu}(\mathbf{p}_i)_{f+}^k \right), \quad (32)$$

$$\boldsymbol{\Sigma}(\mathbf{p}_i)_f^k = \left[\left(\boldsymbol{\Sigma}(\mathbf{p}_i)_{f-}^k \right)^{-1} + \left(\boldsymbol{\Sigma}(\mathbf{p}_i)_{f+}^k \right)^{-1} \right]^{-1}. \quad (33)$$

Next, the weights can be updated as

$$w_f^k = \frac{w_{f-}^k w_{f+}^k}{\sum_{f=1}^F w_{f-}^k w_{f+}^k}. \quad (34)$$

Given (32), (33), (34), the final position estimation can be given by

$$\hat{\mathbf{p}}_i^k = \sum_{f=1}^F w_f^k \boldsymbol{\mu}(\mathbf{p}_i)_f^k. \quad (35)$$

4) *Resampling and Tuning*: Resampling is one of the most crucial steps when performing PGM filtering. Without the resampling step, the filter would suffer from sample depletion. That is, after a while all the gdfs but a few will have negligible weights. Consequently, the posterior will be approximated with only a few gdfs, leading to its underestimation. To overcome this shortcoming, in each iteration we replace the minor-weight gdfs with the new ones whose means are sampled from the approximated posterior. The sample depletion can be monitored throughout the filtering process by calculating the number of effective gdfs as

$$N_{\text{eff}} = \frac{1}{\sum_{f=1}^F (w_f^k)^2}. \quad (36)$$

As can be seen, N_{eff} attains its maximum when all the weights are equal to $\frac{1}{F}$ and falls to its minimum when all but a single weight is equal to zero. In this work, the resampling is carried out when the $N_{\text{eff}} < \frac{2}{3}F$.

Algorithm 1 summarizes the steps required to perform DePF joint sync&loc.

IV. SIMULATION RESULTS AND DISCUSSION

A. DNN-based NLoS Identification

To perform NLoS-identification the DNN in Figure 4 needs to be trained first. The training data is obtained using the QuaDRiGa channel model, details of which are explained in [44]. Specifically, the MU-AP CIRs throughout the MU's movement profile can be implemented under the "3GPP_38.901_UMi" scenario. We collect 5000 CIR realizations for each scenario, i.e., LoS and NLoS, 80% of which is used for the training purpose while the remaining 20% is treated as the test set. To prepare the CIRs to be fed into the DNN, we first input them into a 64-point FFT to obtain the Channel Frequency Responses (CFRs). Subsequently we take the magnitude of the CFRs and normalize each to its maximum component so that all the magnitudes are between 0 and 1. Such normalization is proved to result in a faster learning and convergence [45]. The normalized magnitude of the CFRs are then fed into a DNN with 2 hidden layers, each comprising 50 neurons with Rectified Linear Unit (ReLU) activation function. The loss function in (2) is then optimized using Adam optimizer to obtain the weights of each neuron. Furthermore,

Algorithm 1 DePF joint sync&loc.

-
- 1: Initialize $p(\xi_i^0)$ as in (16).
 - 2: **for all** the APs in \mathcal{I}_i **do**
 - 3: Perform the time-stamp exchange mechanism described in Section II-B2 and Figure 3.
 - 4: Estimate the CIR using QuaDRiGa model.
 - 5: Estimate the AoA and the link condition ζ_{ij}^k using the CIR and (22)
 - 6: **for all** LoS links ζ_{ij}^k **do**
 - 7: Construct \mathbf{B}_{ij}^k , $\mathbf{B}_{ij,f}^k$, \mathbf{R}_{ij}^k , $\mathbf{R}_{ij,f}^k$, \mathbf{r}_{ij}^k and $\mathbf{r}_{ij,f}^k$ by means of the time-stamps and the AoA measurements.
 - 8: Update the parameters of the posterior distribution using (29), (30), (32), and (33).
 - 9: **end for**
 - 10: **end for**
 - 11: Estimate the clock and position parameters using (31) and (35).
 - 12: **if** $N_{\text{eff}} < \frac{2}{3}F$ **then**
 - 13: Perform resampling.
 - 14: **end if**
 - 15: Go to step 2.
-

the probability that a CFR corresponds to a LoS and NLoS link condition is indicated by the DNN's two output neurons with softmax activation function.

Figure 7 depicts the accuracy of the NLoS-identifier based on Support Vector Machine (SVM), a popular classical ML algorithm, and DNN, the method proposed in this work. As can be seen the DNN-based method delivers a higher accuracy, outperforming the classical method. Specifically, DNNs are more powerful when it comes to estimating the classifier function and, therefore, they turn in a superior performance. Moreover, the extremely high accuracy is crucial as determining the link condition is among the most important decisions to be taken. In particular, false detection of NLoS links as LoS, $P_f(\text{LoS})$, not only can result in a poor estimation of the MU position, but also may lead to divergence of the filter. This occurs since the AoA estimation as well as the time-based distance measurement (which in the case of this work is carried out through time-stamp exchange) are highly inaccurate for NLoS links.

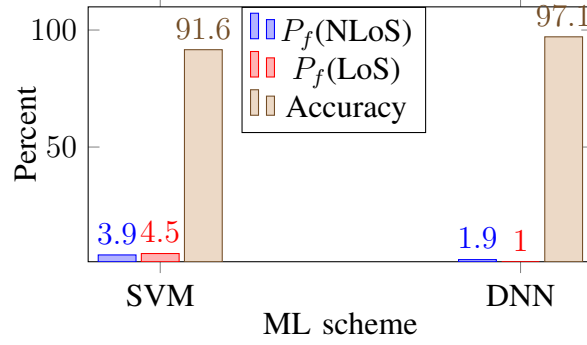


Fig. 7. Comparison of two ML schemes when performing NLoS-identification. $P_f(\text{LoS})/P_f(\text{NLoS})$ denotes the probability that the true condition of the links detected as LoS/NLoS is NLoS/LoS.

B. AoA estimation

To evaluate the performance of the MUSIC algorithm, we arrange a specific simulation setup (shown in Figure 8) where an MU moves with the velocity of 2 m/s along the x axis from the point $[x = 0, y = 0, z = 1.5]$ until $[x = 70, y = 0, z = 1.5]$. An AP with a $N_{\text{ant}} \times N_{\text{ant}}$ UPA and tilted 20° is located at $[x = 35, y = -5, z = 10]$, equally distant from the two edges of the trajectory. Figure 8 depicts such a setup where the MU's trajectory and AP's coverage area (for 23 dBm power allocated to each antenna element) are observable. Furthermore, the elements are assumed to be patch antennas with 90° and 180° beam opening in the elevation and azimuth plane, respectively. Such a setup covers all the possible angles that an MU might have with respect to an AP, i.e. from 6° to 171° . Furthermore, it represents the basic movement of the the MUs in an urban scenario, e.g., the movement profile of the users shown in Figure 1 can be seen as combination of that depicted in Figure 8. Lastly, at each time step, the AoA is estimated using the MUSIC algorithm fed with the corresponding CIR generated by QuaDRiGa.

Figure 9 depicts the Root Mean Square Error (RMSE) of the AoA estimation for several UPA sizes. As can be observed, the RMSE of azimuth AoA estimation remains under 1.5° for almost all the investigated UPAs, what paves the way for a precise localization of the MUs. Nevertheless, in our simulations we observed that for smaller UPAs the RMSE increases drastically due to the large errors at the edges of the trajectory. Although such cases rarely occur, they can potentially lead to the filter divergence. Moreover, the same behavior is observed for the elevation AoA estimation. Generally, as can be seen in the figure, the RMSE is slightly higher for the elevation AoA since the MU is always in the $[10^\circ - 50^\circ]$ angle sight of the AP. We know that UPA's

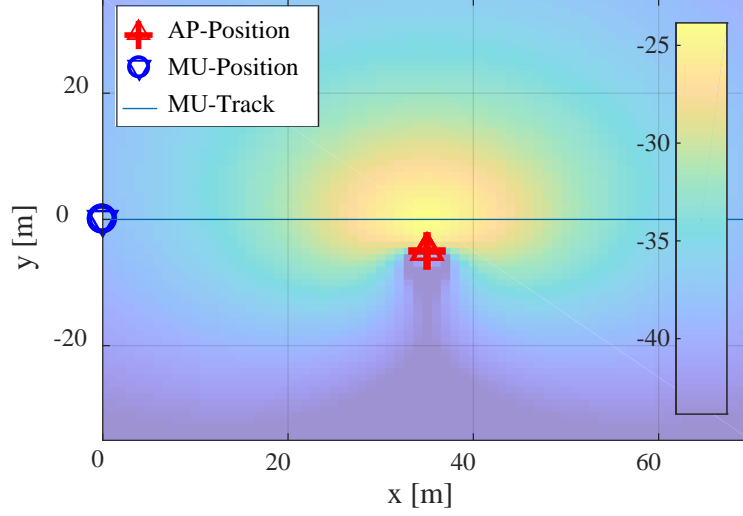


Fig. 8. Simulation setup for calculating the AoA.

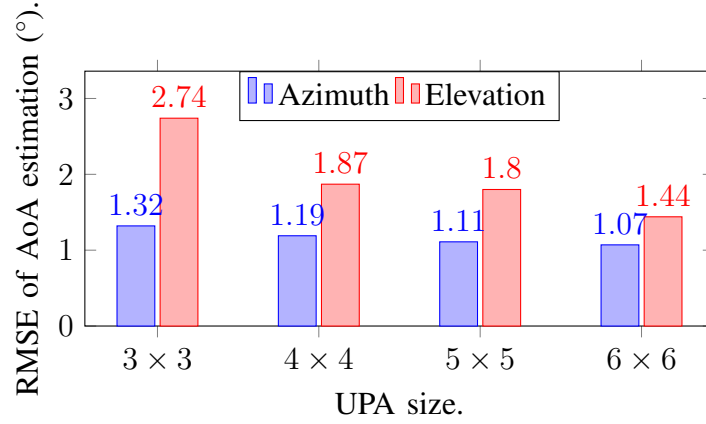


Fig. 9. AoA estimation accuracy.

estimation performance deteriorates as we move towards the edges. In practice, due to the density of APs, the MUs are expected to be in the azimuth angle range of $[20^\circ - 150^\circ]$, and in the elevation angle range of $[20^\circ - 50^\circ]$, i.e., AP density of less than 60 meters.

C. Joint sync&loc

We perform analysis for the scenario shown in Figure 1, which is regarded in [11], [12] as challenging. A car commences its journey by accelerating to reach the velocity of 14 m/s ($= 50$ km/h). It continues moving with constant velocity and decelerates upon approaching the intersection until it completely stops (e.g. due to the red light). The same repeats between the

TABLE I
SIMULATION PARAMETERS

General Parameters	Values
# of independent simulations	1000
Initial random delays ($\tilde{\theta}_i$)	$[-1000, 1000]$ ns
Initial random skew (γ_i)	$[1 - 10^{-3}, 1 + 10^{-3}]$ ns
Max. MU velocity	14 (m/s)
AP density	50 m
Distance traversed by the MU	600 m
QuaDRiGa Parameters	
Scenario	3GPP_38.901_UMi
Center Frequency	3.8 GHz
# of MU/AP antenna (N_{ant})	1 / 3 \times 3
Filter Parameters	
Period of joint sync&loc (T)	100 ms
Process noise covariance matrix (\mathbf{Q}_n)	diag(10^{-5} , 10, 1.5, 1.5)
# of Gaussian mixtures	500
DNN Parameters	
l_H, n_H	2, 50
Optimizer	Adam (lr= 0.001, beta_1=0.9, beta_2=0.999)
# of epochs	10
Batch size	16
Activation function of hidden layers	ReLU
Activation function of output layer	Softmax

two intersections. At the second intersection, it begins moving and takes the turn and continues to accelerate to 14 m/s limit until it exits the map. All the turns as well as acceleration (acc.) coefficients are chosen randomly. During its journey, at each joint sync&loc round k , the MU exchanges time-stamps with a fixed number of APs (N_{AP}) in \mathcal{I}_i , the link to each of which is LoS/NLoS with the probability of 0.8/0.2. The APs are grouped into \mathcal{I}_i based on the distance criteria, that is, \mathcal{I}_i includes the N_{AP} closest APs to the i -th MU. Further assumption is that at each joint sync&loc period T , $N_{\text{ant}} \times N_{\text{ant}}$ CIRs are available at each AP connected to the MU. In our simulations, the CIRs are obtained using the QuaDRiGa channel model. More explicitly, at each round k , knowing the true MU-AP distance and the link condition, i.e., LoS or NLoS, the CIRs are generated using the “3GPP_38.901_UMi” scenario of the QuaDRiGa channel model. Moreover, the RMSEs obtained by [11], [12] serve as the baseline to our approach. The second

scheme with which we compare our proposed algorithm is the L-BRF filtering proposed in [13], [14]. The aforementioned approaches are the most relevant as they draw on the same inputs as our proposed method does.

We initialize all the clock offsets randomly between -1000 and 1000 ns. The initial skews of all the clocks are drawn from the distribution $\mathcal{N}(1, 10^{-3})$. The covariance of clock process noise $\mathbf{Q}_n(\tilde{\boldsymbol{\theta}}_i)$ is set to $\text{diag}(10^{-5}, 100)$ to account for the residual errors from the previous iterations as well as the external noises on the clock skew and offset. The covariance of position process noise $\mathbf{Q}_n(\mathbf{p}_i)$ amounts to $\text{diag}((14T)^2, (14T)^2)$ to account for every possible movement of the MU. All the additional simulation parameters can be found in Table I.

Figure 10 shows the RMSE of clock offset estimation error for three joint sync&loc algorithms. The DePF algorithm is compared with two linear Bayesian methods, i.e., EKF and L-BRF, in multiple scenarios. In particular, we compute the RMSEs in three scenarios, with the number of LoS APs ranging from 1 to 3. In another additional scenario, we consider the MU being connected to three APs, where each MU-AP link condition is set to LoS with the probability of 0.8. As can be seen, for all the LoS scenarios the L-BRF and DePF deliver an identical performance, what is expected as they rely on the same approach to estimate the clock parameters. On the other hand, the performance of the EKF falls behind as it does not explicitly draw on the synchronization signals to estimate the clock offset. Moreover, the synchronization algorithm scheme utilized to synchronize the APs, i.e. hybrid BP-BRF network synchronization, leads to a more precise inter-AP synchronization and, consequently, lowers the MU clock offset estimation error. In the last case, the L-BRF and DePF that are drawing on DNN-based NLoS identification outperform the EKF-based method where the NLoS links are identified by means of Rice factor of the incoming signal strength.

Figure 11 depicts the RMSE of position estimation error for three joint sync&loc algorithms. The DePF algorithm is compared with two linear Bayesian methods, i.e. EKF and L-BRF, in the same scenarios as in Figure 10. As can be seen, for almost all the scenarios the DePF algorithm delivers a superior performance. In particular, since the DePF employs higher number of gdfs, rather than only one, to approximate the posterior distribution, it can estimate the position more accurately. Furthermore, DePF stands out when dealing with NLoS links. This is straightforward to notice as the RMSE of position estimation is lower for DePF in the 3-AP scenario where the L-BRF employs the same NLoS identifier as DePF. Additionally, unlike EKF and L-BRF, DePF does not need any initialization, which is of crucial importance in practice as initialization

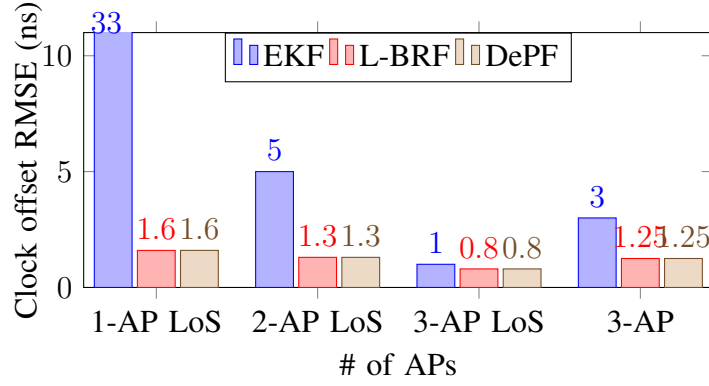


Fig. 10. Performance comparison three joint synchronization and localization algorithms in terms of clock offset estimation.

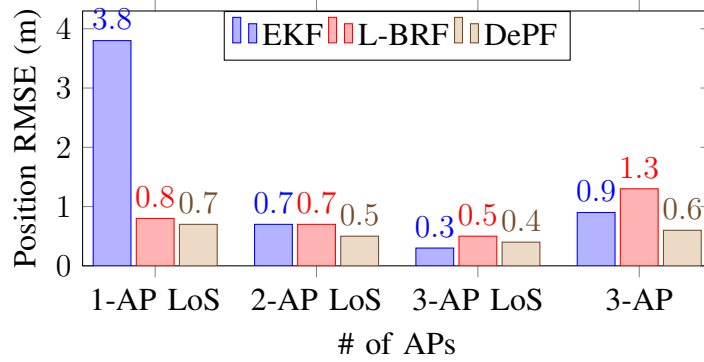


Fig. 11. Performance comparison three joint synchronization and localization algorithms in terms of position estimation.

would require the APs to request position estimation from the MUs, what may not be always possible. Overall, considering 2-AP LoS, 3-AP LoS, and 3-AP scenarios, EKF and L-BRF give a performance close to that of DePF when a reliable initialization and MU-AP links with known LoS condition are available. Nevertheless, such assumptions are questionable in practice, rendering the EKF-based and L-BRF algorithms futile in real-world scenarios.

Hereafter all the simulations have been carried out assuming that there is always at least one LoS MU-AP link. Figure 12 presents the CDF of clock offset estimation error when the MU is connected to multiple number of APs. It can be seen that the estimation accuracy always remains below 2 ns and increases as both L-BRF and DePF utilize more measurements to estimate the clock offset and skew. In fact, since the APs are synchronized with a high precision, collecting time-stamps from each additional AP does provide additional information about the statistics of MU's clock parameters and, therefore, increases the accuracy of the estimation. Such precision

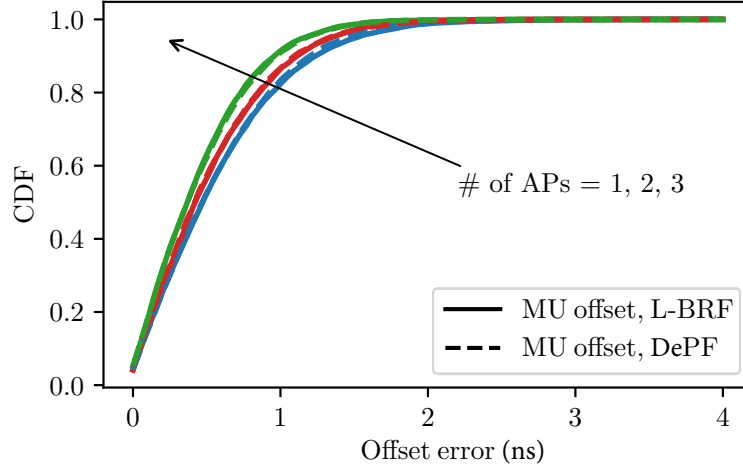


Fig. 12. Performance comparison of L-BRF and DePF when estimating the MUs' clock offset.

is necessary if the location of the MU is to be accurately estimated. We note that each single ns inaccuracy maps to 0.3 m distance measurement error and, consequently, worsens the location estimation. Furthermore, the performance of both schemes are identical as they draw on the same approach to estimate the clock parameters. That is, both model the clock parameters with a single Gaussian function.

Figure 13 presents the CDF of position estimation error when the MU is connected to multiple number of APs. As can be seen, the position estimation error is less than 1 meter in 90% of the cases for the DePF algorithm. We observe that DePF significantly outperforms the L-BRF, especially for 2- and 3-AP scenarios. In particular, unlike the L-BRF that approximates the posterior with a single Gaussian distribution, in DePF the approximation is based on multiple gdfs. Consequently, the approximated posterior is closer to the true one, leading to a more precise position estimation. Another subtle observation is that, although the position estimation error decays with the growth in the number of APs, increasing the number of APs from 2 to 3 only slightly improves the performance. In fact, the third AP is normally far away from the MU, leading to a poorer (AoA and time-stamp) measurement accuracy compared to that of the first two APs. Hence, it does not provide substantial further information about the posterior distribution of the MU's location.

Figure 14 indicates the CDF of position estimation for multiple number of gdfs. It can be noticed that the position estimation ameliorates with the increase of the number of the gdf. This is expected as in PGM filters the posterior distribution is approximated by multiple gdfs.

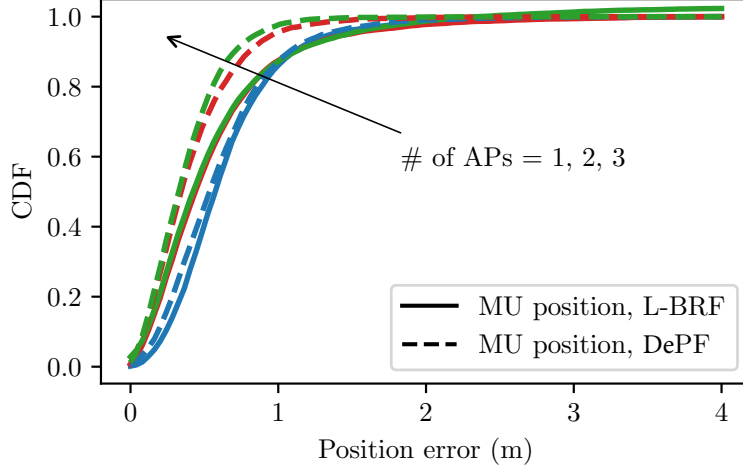


Fig. 13. Performance comparison of L-BRF and DePF when estimating the MUs' position.

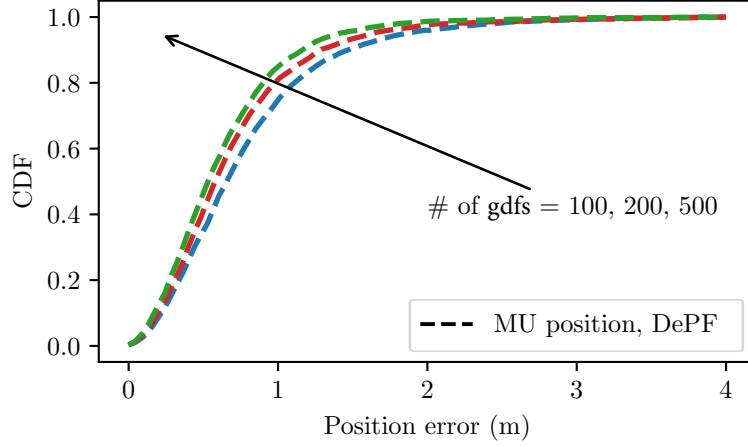


Fig. 14. Performance of joint sync&loc algorithm for different number of gdfs.

Consequently, the more gdfs we employ, the more accuracy we achieve, albeit with higher computation time. Nevertheless, the error reduction is decreasing when increasing the number of gdfs, suggesting that a proper balance needs to be struck between the number of gdfs and the localization accuracy. In the scenarios presented in this work, one can achieve satisfactory performance even with 500 gdfs.

Figure 15 shows the CDF of clock offset estimation error carried out by a single AP for different time-stamp uncertainty, i.e., $\sigma_T = 2, 4, 6$. As can be seen, the clock offset estimation accuracy drops as the σ_T grows. It remains, however, less than 3 ns in 90% of the cases. Such degradation can cause an additional error in position estimation as, given (9), both parameters

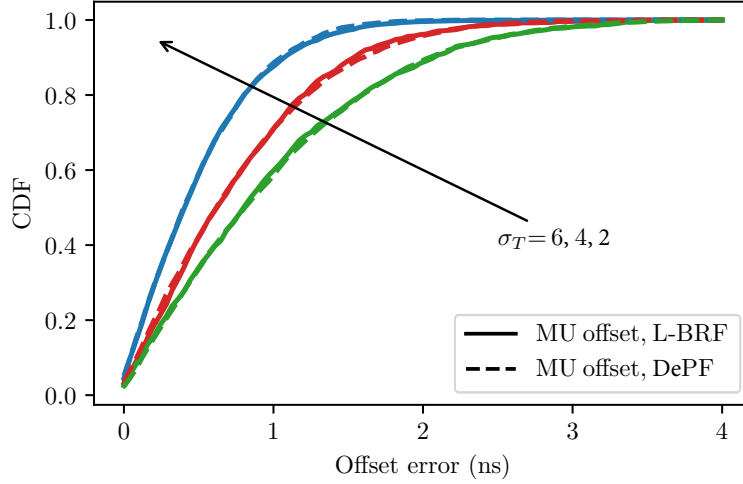


Fig. 15. Clock offset estimation performance of joint sync&loc algorithm with different number of APs involved.

are intertwined. Specifically, offset estimation error can introduce distance measurement error, resulting in imprecision when estimating the position. Nevertheless, the uncertainty of the time-stamping of the state-of-the-art devices are expected to be below 5 ns. Moreover, the destructive impact of the uncertainty can be also mitigated by employing more synchronized APs as discussed previously and shown in Figure 12.

Figure 16 shows the CDF of position estimation conducted by a single AP for different time-stamp accuracies. It can be noticed that the position estimation accuracy deteriorates with the growth in the time-stamp uncertainty. Specifically, the growth in uncertainty results in more erroneous distance measurements and offset estimations, what, consequently, worsens the position estimation accuracy. Nevertheless, it can be readily seen that DePF is more successful in mitigating the destructive effect of the time-stamp uncertainty. Moreover, for both DePF and L-BRF, employing more APs can alleviate the negative impact of large time-stamp uncertainty. In both Figures 15 and 16, it can be noticed that σ_T plays a decisive role in the outcome of the estimation algorithm, what also reveals the importance of hardware components in the design of a robust and precise joint sync&loc algorithm. In practice, such uncertainty in the commercial off-the-shelf devices is expected to be below 5 ns.

In summary, one can see that DNNs can play a decisive role by facilitating the accurate decision-making in simple, albeit crucial, tasks such as NLoS identification. Furthermore, it can be noticed that in the case when we have multiple LoS links available the performance of the

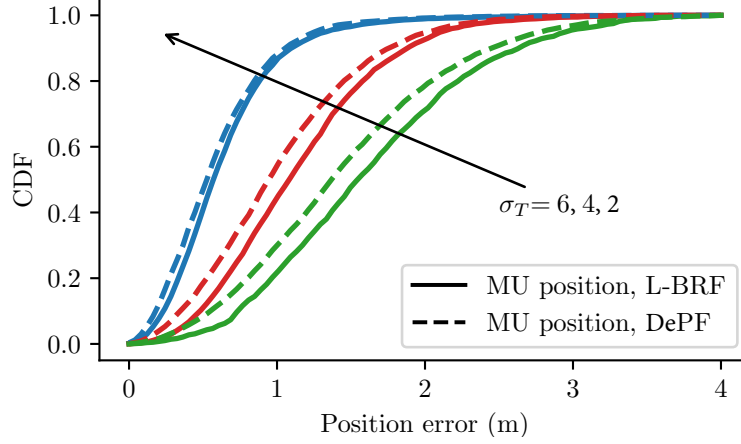


Fig. 16. Position estimation performance of joint sync&loc algorithm with different time-stamp accuracy.

EKF-based and L-BRF approaches both in terms of clock offset and position is close to that of DePF. Nevertheless, in the absence of LoS condition, DePF demonstrates more competence in estimating the clock and position parameters by employing only a few hundreds of gdfs. Another point worth mentioning is that time-stamp exchange is of a high potential to be employed for performing joint sync&loc. In particular, the current communication devices are capable of performing ftm up to 5 ns accuracy, fertilizing the ground for precise offset and distance measurements, which are the basis for a precise joint synchronization and localization.

V. CONCLUSION AND FUTURE WORK

We presented a DNN-assisted Particle-based filtering (DePF) algorithm for joint synchronization and localization (sync&loc) of Mobile Users (MUs) in communication networks. In particular, we leveraged an asymmetric time-stamp exchange mechanism, traditionally utilized for time synchronization, to estimate clock offset and skew while simultaneously obtaining information about the distance between the access points and the MUs. Further on, we combined the aforementioned measurements with angle of arrival estimation and the link condition, i.e. line-of-sight or non-line-of-sight, returned by a pre-trained DNN to localize the MUs. Simulation results indicate that while the performance of the proposed algorithm is promising, especially under the challenging real-world conditions, the position and clock offset estimation errors are dependent on the accuracy of hardware time-stamping. We mitigated the negative impact of this dependency by deploying more access points for performing joint sync&loc.

In this work, we drew on simulations to prove the efficiency of our proposed algorithm. However, to cross-validate the obtained results, the algorithm needs to be implemented in practice. Therefore, in future works, we will employ the hardware at our disposal to evaluate the performance of our proposed joint sync&loc algorithm in practice.

APPENDIX A

Knowing that the measurements are independent and assuming Markov property, we reformulate the integrands in (11) as

$$\begin{aligned} p(\{\mathbf{c}_{ij}^{1:k}, \varphi_{ij}^{1:k}, \zeta_{ij}^{1:k}\}_{\forall j \in \mathcal{I}_i} | \xi_i^0, \dots, \xi_i^k) &= p(\{\mathbf{c}_{ij}^k, \varphi_{ij}^k, \zeta_{ij}^k\}_{\forall j \in \mathcal{I}_i} | \xi_i^k) \cdots p(\{\mathbf{c}_{ij}^1, \varphi_{ij}^1, \zeta_{ij}^1\}_{\forall j \in \mathcal{I}_i} | \xi_i^1), \\ p(\xi_i^0, \dots, \xi_i^k) &= p(\xi_i^k | \xi_i^{k-1}) \cdots p(\xi_i^1 | \xi_i^0) p(\xi_i^0), \end{aligned} \quad (37)$$

where $p(\xi_i^0)$ denotes the prior knowledge on ξ_i . Plugging (37) into (11) leads to (12) where

$$\begin{aligned} p(\xi_i^k | \mathbf{c}_{ij}^{1:k}, \varphi_{ij}^{1:k}, \zeta_{ij}^{1:k}) &\propto \underbrace{\int p(\xi_i^0) \left[\prod_{r=1}^{k-1} p(\xi_i^r | \xi_i^{r-1}) p(\mathbf{c}_{ij}^r, \varphi_{ij}^r, \zeta_{ij}^r | \xi_i^r) \right]}_{=p(\xi_i^k | \mathbf{c}_{ij}^{1:k-1}, \varphi_{ij}^{1:k-1}, \zeta_{ij}^{1:k-1})} p(\xi_i^k | \xi_i^{k-1}) \times p(\mathbf{c}_{ij}^k, \varphi_{ij}^k, \zeta_{ij}^k | \xi_i^k), \end{aligned} \quad (38)$$

REFERENCES

- [1] Y.-C. Wu, Q. Chaudhari, and E. Serpedin, "Clock synchronization of wireless sensor networks," *IEEE Signal Processing Magazine*, vol. 28, no. 1, pp. 124–138, 2010.
- [2] N. Maletic, V. Sark, J. Gutiérrez, and E. Grass, "Device localization using mmwave ranging with sub-6-assisted angle of arrival estimation," in *2018 IEEE International Symposium on Broadband Multimedia Systems and Broadcasting (BMSB)*. IEEE, 2018, pp. 1–6.
- [3] "IEEE standard for information technology—telecommunications and information exchange between systems local and metropolitan area networks—specific requirements - part 11: Wireless LAN Medium Access Control (MAC) and physical layer (PHY) specifications," *IEEE Std 802.11-2016 (Revision of IEEE Std 802.11-2012)*, pp. 1–3534, 2016.
- [4] W. Yuan, N. Wu, B. Etzlinger, H. Wang, and J. Kuang, "Cooperative joint localization and clock synchronization based on gaussian message passing in asynchronous wireless networks," *IEEE Transactions on Vehicular Technology*, vol. 65, no. 9, pp. 7258–7273, 2016.
- [5] B. Etzlinger, F. Meyer, F. Hlawatsch, A. Springer, and H. Wymeersch, "Cooperative simultaneous localization and synchronization in mobile agent networks," *IEEE Transactions on Signal Processing*, vol. 65, no. 14, pp. 3587–3602, 2017.
- [6] F. Meyer, B. Etzlinger, Z. Liu, F. Hlawatsch, and M. Z. Win, "A scalable algorithm for network localization and synchronization," *IEEE Internet of Things Journal*, vol. 5, no. 6, pp. 4714–4727, 2018.
- [7] S. P. Chepuri, R. T. Rajan, G. Leus, and A.-J. van der Veen, "Joint clock synchronization and ranging: Asymmetrical time-stamping and passive listening," *IEEE Signal Processing Letters*, vol. 20, no. 1, pp. 51–54, 2012.

- [8] R. M. Vaghefi and R. M. Buehrer, "Cooperative joint synchronization and localization in wireless sensor networks," *IEEE Transactions on Signal Processing*, vol. 63, no. 14, pp. 3615–3627, 2015.
- [9] M. Goodarzi, D. Cvetkovski, N. Maletic, J. Gutiérrez, and E. Grass, "A hybrid bayesian approach towards clock offset and skew estimation in 5g networks," in *2020 IEEE 31st Annual International Symposium on Personal, Indoor and Mobile Radio Communications*. IEEE, 2020, pp. 1–7.
- [10] —, "Synchronization in 5g: a bayesian approach," in *2020 European Conference on Networks and Communications (EuCNC)*. IEEE, 2020, pp. 194–199.
- [11] J. Werner, M. Costa, A. Hakkarainen, K. Leppanen, and M. Valkama, "Joint user node positioning and clock offset estimation in 5G ultra-dense networks," in *2015 IEEE Global Communications Conference (GLOBECOM)*. IEEE, 2015, pp. 1–7.
- [12] M. Koivisto, M. Costa, J. Werner, K. Heiska, J. Talvitie, K. Leppänen, V. Koivunen, and M. Valkama, "Joint device positioning and clock synchronization in 5g ultra-dense networks," *IEEE Transactions on Wireless Communications*, vol. 16, no. 5, pp. 2866–2881, 2017.
- [13] M. Goodarzi, N. Maletic, J. Gutiérrez, and E. Grass, "Bayesian joint synchronization and localization based on asymmetric time-stamp exchange," in *2020 International Symposium on Networks, Computers and Communications (ISNCC)*. IEEE, 2020, pp. 1–7.
- [14] M. Goodarzi, D. Cvetkovski, N. Maletic, J. Gutiérrez, and E. Grass, "Synchronization in 5g networks: a hybrid bayesian approach toward clock offset/skew estimation and its impact on localization," *EURASIP Journal on Wireless Communications and Networking*, vol. 2021, no. 1, pp. 1–22, 2021.
- [15] A. S. Stordal, H. A. Karlsen, G. Nævdal, H. J. Skaug, and B. Vallès, "Bridging the ensemble kalman filter and particle filters: the adaptive gaussian mixture filter," *Computational Geosciences*, vol. 15, no. 2, pp. 293–305, 2011.
- [16] D. Alspach and H. Sorenson, "Nonlinear bayesian estimation using gaussian sum approximations," *IEEE transactions on automatic control*, vol. 17, no. 4, pp. 439–448, 1972.
- [17] F. Gustafsson, "Particle filter theory and practice with positioning applications," *IEEE Aerospace and Electronic Systems Magazine*, vol. 25, no. 7, pp. 53–82, 2010.
- [18] I. Guvenc and C.-C. Chong, "A survey on toa based wireless localization and nlos mitigation techniques," *IEEE Communications Surveys & Tutorials*, vol. 11, no. 3, pp. 107–124, 2009.
- [19] K. Yu and E. Dutkiewicz, "Nlos identification and mitigation for mobile tracking," *IEEE Transactions on Aerospace and electronic systems*, vol. 49, no. 3, pp. 1438–1452, 2013.
- [20] S. Venkatraman and J. Caffery, "Statistical approach to non-line-of-sight bs identification," in *The 5th International Symposium on Wireless Personal Multimedia Communications*, vol. 1. IEEE, 2002, pp. 296–300.
- [21] S. Marano, W. M. Gifford, H. Wymeersch, and M. Z. Win, "Nlos identification and mitigation for localization based on uwb experimental data," *IEEE Journal on selected areas in communications*, vol. 28, no. 7, pp. 1026–1035, 2010.
- [22] F. Xiao, Z. Guo, H. Zhu, X. Xie, and R. Wang, "Ampn: Real-time los/nlos identification with wifi," in *2017 IEEE International Conference on Communications (ICC)*. IEEE, 2017, pp. 1–7.
- [23] J. Heaton, *Introduction to neural networks with Java*. Heaton Research, Inc., 2008.
- [24] R. Schmidt, "Multiple emitter location and signal parameter estimation," *IEEE transactions on antennas and propagation*, vol. 34, no. 3, pp. 276–280, 1986.
- [25] X. Zhang, L. Xu, L. Xu, and D. Xu, "Direction of departure (DOD) and direction of arrival (DOA) estimation in MIMO radar with reduced-dimension MUSIC," *IEEE communications letters*, vol. 14, no. 12, pp. 1161–1163, 2010.
- [26] R. Roy and T. Kailath, "ESPRIT-estimation of signal parameters via rotational invariance techniques," *IEEE Transactions on acoustics, speech, and signal processing*, vol. 37, no. 7, pp. 984–995, 1989.

- [27] O. A. Oumar, M. F. Siyau, and T. P. Sattar, "Comparison between music and esprit direction of arrival estimation algorithms for wireless communication systems," in *The First International Conference on Future Generation Communication Technologies*. IEEE, 2012, pp. 99–103.
- [28] J. Eidson and K. Lee, "IEEE 1588 standard for a precision clock synchronization protocol for networked measurement and control systems," in *Sensors for Industry Conference, 2002. 2nd ISA/IEEE*. Ieee, 2002, pp. 98–105.
- [29] B. Mondal, T. A. Thomas, E. Visotsky, F. W. Vook, A. Ghosh, Y.-H. Nam, Y. Li, J. Zhang, M. Zhang, Q. Luo *et al.*, "3d channel model in 3gpp," *IEEE Communications Magazine*, vol. 53, no. 3, pp. 16–23, 2015.
- [30] B. Etzlinger, H. Wymeersch, and A. Springer, "Cooperative synchronization in wireless networks," *IEEE Transactions on Signal Processing*, vol. 62, no. 11, pp. 2837–2849, 2014.
- [31] M. Leng and Y.-C. Wu, "Distributed clock synchronization for wireless sensor networks using belief propagation," *IEEE Transactions on Signal Processing*, vol. 59, no. 11, pp. 5404–5414, 2011.
- [32] G. Giorgi and C. Narduzzi, "Performance analysis of kalman-filter-based clock synchronization in IEEE 1588 networks," *IEEE Transactions on Instrumentation and Measurement*, vol. 60, no. 8, pp. 2902–2909, 2011.
- [33] J. Du and Y.-C. Wu, "Distributed clock skew and offset estimation in wireless sensor networks: Asynchronous algorithm and convergence analysis," *IEEE Transactions on Wireless Communications*, vol. 12, no. 11, pp. 5908–5917, 2013.
- [34] "AI and ML – enablers for beyond 5G networks," 2021. [Online]. Available: <http://doi.org/10.5281/zenodo.4299895>
- [35] W. Liu, Z. Wang, X. Liu, N. Zeng, Y. Liu, and F. E. Alsaadi, "A survey of deep neural network architectures and their applications," *Neurocomputing*, vol. 234, pp. 11–26, 2017.
- [36] S. Boyd, S. P. Boyd, and L. Vandenberghe, *Convex optimization*. Cambridge university press, 2004.
- [37] J. Chen, S. Guan, Y. Tong, and L. Yan, "Two-dimensional direction of arrival estimation for improved archimedean spiral array with music algorithm," *IEEE Access*, vol. 6, pp. 49 740–49 745, 2018.
- [38] F.-G. Yan, Z.-K. Chen, M.-J. Sun, Y. Shen, and M. Jin, "Two-dimensional direction-of-arrivals estimation based on one-dimensional search using rank deficiency principle," *International Journal of Antennas and Propagation*, vol. 2015, 2015.
- [39] M. Mohanna, M. L. Rabeh, E. M. Zieur, and S. Hekala, "Optimization of music algorithm for angle of arrival estimation in wireless communications," *NRIAG journal of Astronomy and Geophysics*, vol. 2, no. 1, pp. 116–124, 2013.
- [40] V. Mihajlovic and M. Petkovic, "Dynamic bayesian networks: A state of the art," *University of Twente Document Repository*, 2001.
- [41] A. L. Barker, D. E. Brown, and W. N. Martin, "Bayesian estimation and the kalman filter," *Computers & Mathematics with Applications*, vol. 30, no. 10, pp. 55–77, 1995.
- [42] R. Khan, S. U. Khan, S. Khan, and M. U. A. Khan, "Localization performance evaluation of extended kalman filter in wireless sensors network," *Procedia Computer Science*, vol. 32, pp. 117–124, 2014.
- [43] R. Labbe, "Kalman and bayesian filters in python, 2014," 2019. [Online]. Available: <https://github.com/rlabbe/Kalman-and-Bayesian-Filters-in-Python>
- [44] S. Jaeckel, L. Raschkowski, K. Börner, and L. Thiele, "Quadriga: A 3-d multi-cell channel model with time evolution for enabling virtual field trials," *IEEE Transactions on Antennas and Propagation*, vol. 62, no. 6, pp. 3242–3256, 2014.
- [45] J. Shao, K. Hu, C. Wang, X. Xue, and B. Raj, "Is normalization indispensable for training deep neural network?" *Advances in Neural Information Processing Systems*, vol. 33, 2020.